

## Article

# Optical Turbulence Profile in Marine Environment with Artificial Neural Network Model

Cuicui Bi <sup>1,2,3</sup>, Chun Qing <sup>1,3,\*</sup>, Pengfei Wu <sup>1,3</sup>, Xiaomei Jin <sup>1,3</sup>, Qing Liu <sup>1,3</sup>, Xianmei Qian <sup>1,3</sup>, Wenyue Zhu <sup>1,3</sup> and Ningquan Weng <sup>1,3</sup>

<sup>1</sup> Key Laboratory of Atmospheric Optics, Anhui Institute of Optics and Fine Mechanics, Hefei Institutes of Physical Science, Chinese Academy of Sciences, Hefei 230031, China; cuibi168@mail.ustc.edu.cn (C.B.); wupengfei@aiofm.ac.cn (P.W.); xmjin@aiofm.ac.cn (X.J.); liuqing@aiofm.ac.cn (Q.L.); qianxianmei@aiofm.ac.cn (X.Q.); zhuwenyue@aiofm.ac.cn (W.Z.); wnq@aiofm.ac.cn (N.W.)

<sup>2</sup> Science Island Branch of Graduate School, University of Science and Technology of China, Hefei 230026, China

<sup>3</sup> Advanced Laser Technology Laboratory of Anhui Province, Hefei 230037, China

\* Correspondence: chunqing@aiofm.ac.cn

**Abstract:** Optical turbulence strongly affects different types of optoelectronic and adaptive optics systems. Systematic direct measurements of optical turbulence profiles [ $C_n^2(h)$ ] are lacking for many climates and seasons, particularly in marine environments, because it is impractical and expensive to deploy instrumentation. Here, a backpropagation neural network optimized using a genetic algorithm (GA-BP) is developed to estimate atmospheric turbulence profiles in marine environments which is validated against corresponding [ $C_n^2(h)$ ] profile datasets from a field campaign of balloon-borne microthermal measurements at the Haikou marine environment site. Overall, the trend and magnitude of the GA-BP model and measurements agree. The [ $C_n^2(h)$ ] profiles from the GA-BP model are generally superior to those obtained by BP and the physically-based (HMNSP99) models. Several statistical operators were used to quantify the GA-BP model performance on reconstructing the optical turbulence profiles in marine environments. The characterization of vertical distributions of optical turbulence profiles and the main integral parameters derived from [ $C_n^2(h)$ ] profiles are presented. The median Fried parameter, isoplanatic angle, and coherence time are 9.94 cm, 0.69'', and 2.85 ms, respectively, providing independent optical turbulence parameters for adaptive optics systems. The proposed approach exhibits potential for implementation in ground-based optical applications in marine environments.



**Citation:** Bi, C.; Qing, C.; Wu, P.; Jin, X.; Liu, Q.; Qian, X.; Zhu, W.; Weng, N. Optical Turbulence Profile in Marine Environment with Artificial Neural Network Model. *Remote Sens.* **2022**, *14*, 2267. <https://doi.org/10.3390/rs14092267>

Academic Editor: Michael E. Gorbunov

Received: 25 March 2022

Accepted: 5 May 2022

Published: 8 May 2022

**Publisher's Note:** MDPI stays neutral with regard to jurisdictional claims in published maps and institutional affiliations.



**Copyright:** © 2022 by the authors. Licensee MDPI, Basel, Switzerland. This article is an open access article distributed under the terms and conditions of the Creative Commons Attribution (CC BY) license (<https://creativecommons.org/licenses/by/4.0/>).

## 1. Introduction

Optical turbulence within the atmosphere of the Earth plays a significant role in optoelectronic systems (e.g., laser communication, target detection, and astronomical observation). In particular, in marine environments, the turbulent effects strongly restrict the performance of electro-optical engineering, such as optical remote sensing imaging, free-space optical communication, and laser propagation in the atmosphere. Therefore, obtaining accurate optical turbulence profiles is essential for guiding the design of adaptive optical systems, improving the imaging quality and performance of photoelectric systems.

The refractive index structure constant,  $C_n^2$ , has been used as an indicator to characterize and quantify the turbulent spatial fluctuations caused by temperature gradients [1,2], wherein  $n$  denotes the local refractive index of the atmosphere. Existing techniques for  $C_n^2$  measurements include scintillation detection and ranging (SCIDAR) [3], multi-aperture scintillation sensor (MASS) [4,5], scintillator [6], Shack Hartmann wavefront sensor (SHWFS) [7–13], Differential Image Motion (DIM) Light Detection and Ranging (LIDAR) [14], acoustic meteorological radar (sodar) [15], and the balloon-borne microthermometry [16]. Indeed, various techniques exist for the measurement of  $C_n^2(h)$ . How-

ever, for logistical and financial issues, obtaining longterm and large-scale  $C_n^2$  data using instruments is unavailable, particularly in marine environments. Therefore, establishing the relationship between conventional meteorological parameters and  $C_n^2$  has become an essential part of atmospheric optical turbulence model research. Hufnagel summarized the upper altitude atmospheric turbulence parameter model which considers the wind speed [17]. However, the mode had a limited altitude range of use. The fundamental theories for estimating atmospheric turbulence were presented by Tatarskii [1]. According to Tatarskii optical turbulence estimation theory, Abahamid explored the optical turbulence modeling in the boundary layer and free atmosphere using instrumented meteorological balloons from nine sites [18]. Similarly, Nath performed a correlation analysis by using three years of high-resolution radiosonde data over the tropical station Gadanki to study the relative contributions of temperature and relative humidity to the refractive index gradient [19]. It is well known that atmospheric turbulence depends largely on background atmospheric parameters, such as wind, temperature, and humidity. Subsequently, various outer scale models for calculating  $C_n^2$  using conventional meteorological parameters based on Tatarskii theory have been developed, including the Dewan model [20], HMNSP99 model [21], and Thorpe model [22]. Notably, the HMNSP99 model is more popular for estimating, and it has a similar structure to the Dewan model; however, it contains temperature gradients in addition to wind shear. Although different parameterization models were presented, quasi-universality was limited to certain areas, and none of them are known to be superior.

Furthermore, optical turbulence has variability in different regions. The estimated results from the physically-based models are unsatisfactory. So, it is necessary to perform measurements and new estimated model research. The artificial neural network (ANN) has been widely used as a powerful tool to handle big data, which is primarily due to the flexibility of the technique. The technique relies on the ability of ANN to successfully learn directly from the data of the real problem and adjust to complex models with ease, allowing ANN to be applied in different research fields [23–27]. Importantly, ANN delivers outstanding predictive performance without any a priori assumptions. Moreover, Wang utilized a neural network to estimate surface-layer optical turbulence in the Mauna Loa Observatory for one month with five conventional meteorological parameters, initially confirming the feasibility of this method [28]. Su proposed a new artificial neural network approach to estimate surface-layer optical turbulence over the Antarctic [29], and further explain the feasibility of the new  $C_n^2$  quantification method. In addition to avoiding the complicated physical calculation process in the Monin–Obukhov similarity theory, the ANN method also proves the potential for estimating near-surface under different stability conditions. Furthermore, Xu used backpropagation neural networks to estimate offshore atmospheric boundary layer vertical  $C_n^2$  profiles [30].

This work proposes a novel hybrid neural network that combines the back propagation (BP) neural network and the genetic algorithm (GA) to estimate  $C_n^2(h)$  profiles in marine environments. Additionally, this study presents the new neural network model developed on this data set and compared it with the HMNSP99 model (Holloman Spring1999 thermosonde campaigns, developed and tested by the Air Force Research Laboratory), and the results show that the GA-BP neural network model can perform with better accuracy with respect to the corresponding radiosonde data compared to BP and the Tatarskii physically-based models.

The remainder of this study is organized as follows: methodology of GA-BP and HMNSP99 models are introduced in Section 2. Section 3 provides the detailed principle of in situ balloon-borne microthermal measurements and data. The model results of  $C_n^2(h)$  profiles are shown in Section 4. Lastly, the discussion and conclusions are presented in Sections 5 and 6.

## 2. Methodology

### 2.1. GA-BP Model

Atmospheric turbulence generates local inhomogeneities in the atmosphere, particularly for the spatial inhomogeneities of temperature. Meanwhile, seasons and weather factors affect the turbulence intensity, which has significantly different characteristics in  $C_n^2(h)$  vertical profiles. Admittedly, many researchers have proposed different models to estimate atmospheric turbulence, each model is empirical and has limitations. However, modeling the relationship between atmospheric turbulence and other meteorological variables can be interpreted as a nonlinear regression problem. ANN has the advantages of flexible nonlinear modeling capability, strong adaptability, and their learning and massively parallel computing abilities. In addition, ANN can learn and obtain useful information from input and output data without establishing precise mathematical models. The back-propagation (BP) neural network is a critical realization method of ANNs, also known as the error back propagation network. The BP neural network is a multilayer mapping network that minimizes an error backward while the information is transmitted forward. In the training process, each connection weight and threshold are adjusted in turn for iterative training based on the error between the output and desired goal until the preset error goal or the maximum iterations (this study set the maximum iterations to 1000) are reached. Generally, the BP neural network with a single hidden layer can approximate any nonlinear function with arbitrary precision, which makes the BP neural network suitable for dealing with complex nonlinear problems [31]. However, the randomness of initialization weights and thresholds of the BP neural network makes the results fall into local extremes rather than into the global optimum. Furthermore, the network has the disadvantage of poor robustness and slow training speed. To overcome this shortcoming, this study proposes adopting the genetic algorithm to optimize the initial connection weights and thresholds of the BP neural network, improving the ability of convergence speed or prediction accuracy.

This study establishes the mapping relationship between the conventional meteorological parameters and  $C_n^2$ . The topological structural diagram of the GA-BP model consists of an input layer, a hidden layer, and an output layer as shown in Figure 1.

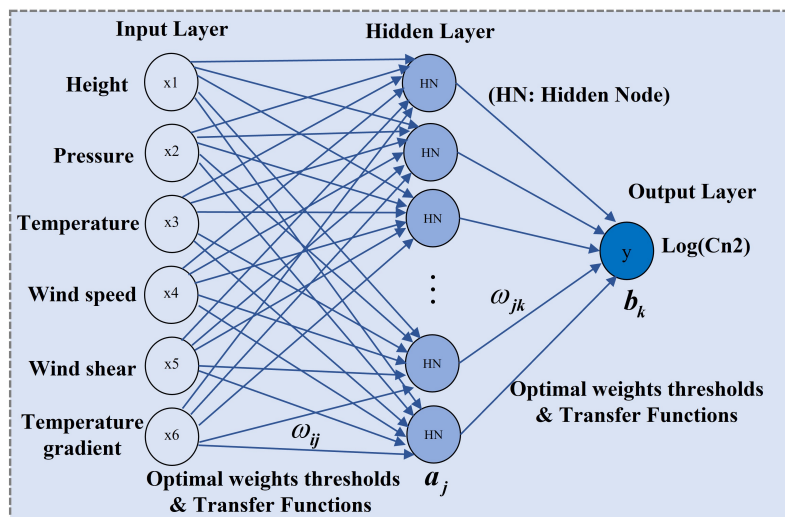


**Figure 1.** Topological structure diagram of the GA-BP neural network model.

According to the structure diagram,  $X_1, X_2, \dots, X_6$  denote the input values,  $Y$  denotes the target output, and adjacent layers are connected by weights ( $\omega_{ij}, \omega_{jk}$ ).  $a_j$  and  $b_k$  are thresholds of the hidden layer and output layer, respectively. The input layer parameters contain six meteorological parameters (height, pressure, temperature, wind speed, wind shear, and temperature gradient), which are closely related to optical turbulence. Notably, the altitude parameter presents the spatial information of atmospheric turbulence. Moreover,  $\log[C_n^2(h)]$  is the target output parameter. However, the number of the hidden

layer depends on the degree of nonlinear mapping between input and output parameters, and increasing the hidden nodes does not necessarily improve the model performance all the time [32]. On the one hand, a lack of neurons in the hidden layer will lead to poor prediction accuracy resulting from the under-fitting problem. On the other hand, too many neurons will lead to over-fitting, generating large generation errors. Wherein there is no standard and specific theoretical guidance to determine the number of hidden neurons. Experiments or by trial and error based on the data are the most common means to ascertain the appropriate number of hidden nodes.

In this study, the cross-validation method is used to realize the trade-off between the accuracy of the training set and the generalization ability of the validation set for a different number of hidden neurons. All the training data are from 123 observational meteorological sounding profiles data in the marine environment. Consider the morning training process as an example, training data are randomly split into three disjoint sets [training set (60%), validation set (20%), and testing set (20%)]. All data during the training progress needed to be normalized to  $[-1, 1]$  to eliminate the interference of different units in network training. The training function of the network corresponds to the resilient back propagation algorithm [33]. The training set is used to train the model and present the training error, whereas the validation set is used to select the number of hidden neurons. For the increased number of hidden neurons, the performances of the training and validation sets are evaluated using the mean relative error operator. Figure 2 illustrates the mean relative error of the training and validation for different numbers of hidden neurons. Obviously, the average relative errors of the training and validation sets are small while the number of neurons is 30, which repeatedly runs with the same training parameters. Therefore, the input layer ( $M$ ) has six input factors, the hidden layer ( $l$ ) is one layer and contains 30 neurons, and the output layer ( $m$ ) is  $\log[C_n^2(h)]$ .

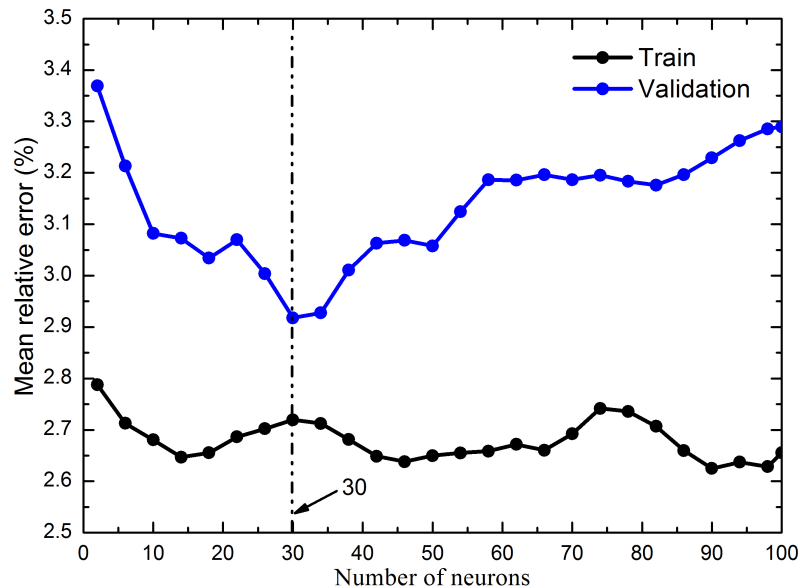


**Figure 2.** Mean relative error of the training and validation for different numbers of hidden neurons.

The flowchart of the proposed GA-BP neural network model is shown in Figure 3, which comprises two parts: genetic algorithm (left) and back propagation algorithm (right). GA-BP is adopted for improving the training speed and robustness of the BP neural network model. The procedures of the optimized algorithm are as follows:

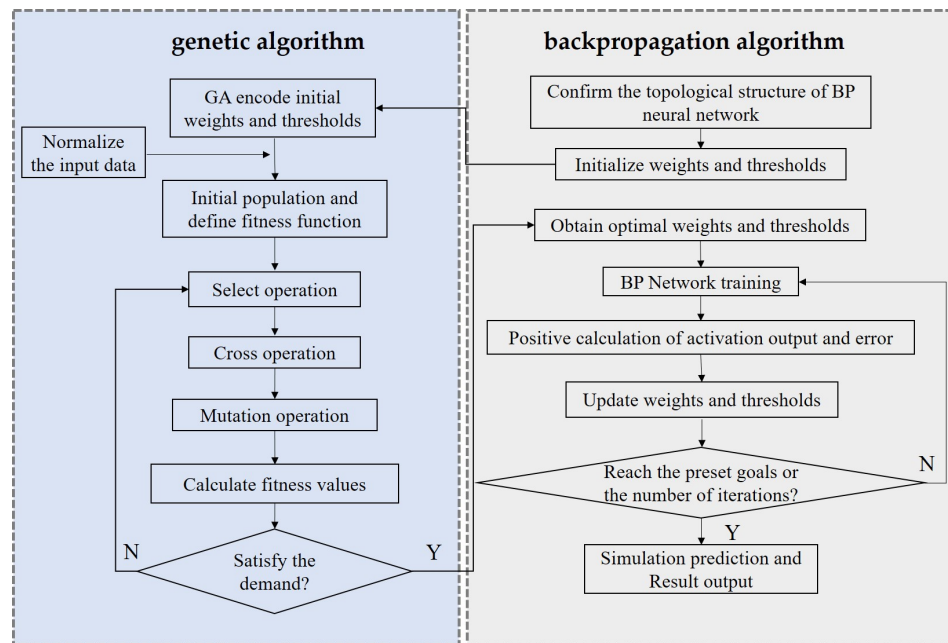


**Figure 3.** Algorithm flowchart of the GA-BP neural network model.

1. Confirm the topological structure of GA-BP neural network ( $M-l-m$ ) and normalize the original data.

$$x = \frac{2(X - X_{min})}{(X_{max} - X_{min})} - 1, \quad (1)$$

where  $x$  denotes the normalized parameters' values, which are within the range  $[-1, 1]$ .  $X_{min}$  and  $X_{max}$  are the minimum and maximum values of the original parameters data, respectively.

2. Code the generation and initialize the population. The random weights  $\omega_{ij}$ ,  $\omega_{jk}$  and thresholds  $a_j$ ,  $b_k$  are expressed as chromosome data in the genetic space for coding. Chromosomes containing genetic information are randomly generated, and each data is called an individual, which represents feasible solutions. Genes, namely genetic information, represent components of feasible solutions. The individuals constitute the initial population. Additionally, the length of the Chromosome ( $C$ ) can be acquired by the number of the input layer ( $M$ ), the hidden layer ( $l$ ), and the number of output layer ( $m$ ).

$$C = M * l + l * m + l + m, \quad (2)$$

3. Fitness assessment. Calculate the fitness ( $F$ ) of the individual, which is based on the mean absolute error between the actual values and the network output values.

$$F = \frac{1}{\sum_{i=1}^N \frac{|V_i - A_i|}{N}}, \quad (3)$$

where  $V_i$  denotes the actual values,  $A_i$  denotes the output of the network.  $N$  represents the number of training samples. The smaller the mean absolute error, the higher the fitness level.

4. Selection, Crossover and Mutation operations: select good individuals from the current population to enter the next generation based on fitness; generate new individuals by using the crossover operation, which combines the characteristics of the parents; the values of chromosomal genes randomly change by mutation operation, providing opportunities for new individuals to emerge.
5. The optimal values from GA are assigned as the initial connection weights and thresholds of the BP neural network.

6. Calculate the output results of the hidden layer ( $H_j$ ).  $H_j$  can be obtained from the input vector  $x$ , the connection weight  $\omega_{ij}$  between the input layer  $M$  and the hidden layer  $l$ , and the hidden layer threshold  $a_j$ .

$$H_j = f \left( \sum_{i=1}^M \omega_{ij} x_i - a_j \right), \quad j = 1, 2, \dots, l \quad (4)$$

where  $l$  denotes the number of hidden layer nodes.  $f$  represents the activation function and commonly used sigmoid function as the activation function in GA-BP neural network.

$$f = \frac{1}{1 + e^{-x}}, \quad (5)$$

7. Calculate the results of the network output layer ( $O_k$ ).  $O_k$  can be calculated based on the output of the hidden layer  $H$ , connection weights  $\omega_{jk}$ , and thresholds  $b_k$ .

$$O_k = \sum_{j=1}^l H_j \omega_{jk} - b_k, \quad k = 1, 2, \dots, m \quad (6)$$

8. Calculate network error ( $e_k$ ). The  $e_k$  can be calculated by actual results values ( $Y_k$ ) and the network output results ( $O_k$ ).

$$e_k = Y_k - O_k, \quad k = 1, 2, \dots, m \quad (7)$$

9. Update weights of the network ( $\omega_{ij}, \omega_{jk}$ ) according to the network error  $e$ .

$$\omega_{ij} = \omega_{ij} + \eta H_j (1 - H_j) x(i) \sum_{k=1}^m \omega_{jk} e_k, \quad i = 1, 2, \dots, M; \quad j = 1, 2, \dots, l \quad (8)$$

$$\omega_{jk} = \omega_{jk} + \eta H_j e_k, \quad k = 1, 2, \dots, m \quad (9)$$

where  $\eta$  is the learning rate.

10. Update thresholds of the network ( $a_j, b_k$ ) based on the network error  $e$ .

$$a_j = a_j + \eta H_j (1 - H_j) x(i) \sum_{k=1}^m \omega_{jk} e_k, \quad j = 1, 2, \dots, l \quad (10)$$

$$b_k = b_k + e_k, \quad k = 1, 2, \dots, m \quad (11)$$

11. If the algorithm reaches the preset goals or reaches the number of iterations, then the network is trained with the training sample; thus, the best-fitting network is created.  
 12. The network is applied to forecast the test samples.

The hyperparameter settings of the GA-BP neural network are determined based on the network mechanism. The population size is 50, the number of maximum generation is 100, and the crossover rate and mutation rate are 0.5 and 0.06, respectively. Figure 4 presents the training process of the GA-BP model to optimize the initial weights and thresholds of the neural network in the morning. As the number of generations increases, the best fitness and the average fitness level increase gradually stabilize. The optimal fitness value is 6.63 when the number of generations reaches 53 generations, which indicates that the corresponding weights and thresholds reach the best.

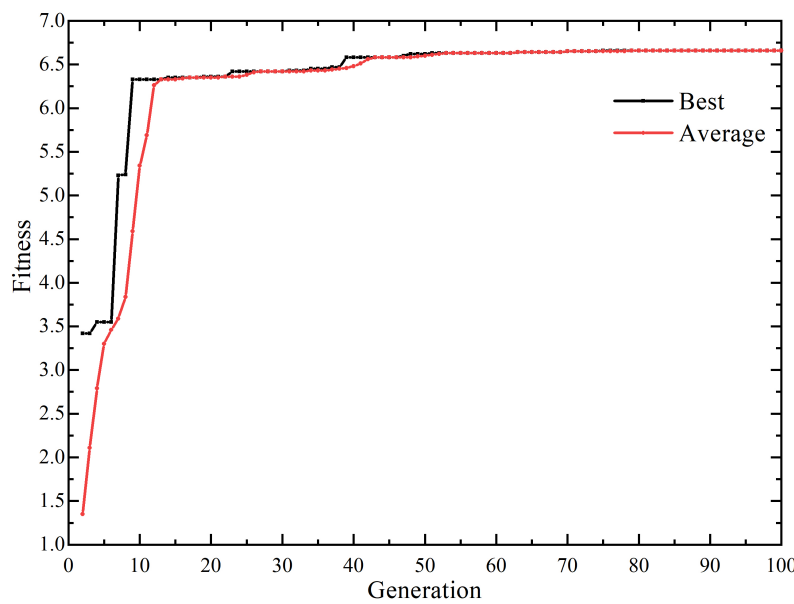


**Figure 4.** Training process of the GA-BP neural network model.

## 2.2. Physically-Based Model

The optical turbulence profile estimation model (Tatarskii model) is used to convert standard meteorological data into  $C_n^2(h)$  vertical profiles, and the estimation model has been used to forecast optical seeing conditions for ground-based telescopes. Under the assumption that the turbulence follows the Kolmogorov hypothesis, the Tatarskii model has the following form [1]:

$$C_n^2 = 2.8 \left[ \frac{79 \times 10^{-6} P}{T^2} \left( \frac{dT}{dh} + \gamma \right) \right]^2 L_0^{4/3}, \quad (12)$$

where  $T$  denotes the absolute atmospheric temperature in K,  $P$  indicates the pressure in hPa,  $\gamma$  denotes the dry adiabatic lapse rate ( $9.8 \times 10^3$  K/m),  $h$  denotes the height above ground.  $L_0$  indicates the outer scale of atmospheric turbulence. These parameters can be obtained from the sounding. However, the outer scale  $L_0$  model is controversial. Ruggiero summarized the HMNSP99 model based on a large volume of experimental data [21]. The HMNSP99 model contains additional atmospheric parameters besides the wind shear, the temperature gradient is also commonly used to estimate atmospheric turbulence, which can be expressed as

$$L_0^{4/3} = \begin{cases} 0.1^{4/3} \times 10^{0.362+16.728S-192.347\frac{dT}{dh}}, & \text{Troposphere} \\ 0.1^{4/3} \times 10^{0.757+13.819S-57.784\frac{dT}{dh}}, & \text{Stratosphere} \end{cases} \quad (13)$$

where  $S$  denotes the vertical shear of horizontal velocity, which is defined as

$$S = \sqrt{\left( \frac{\partial u}{\partial h} \right)^2 + \left( \frac{\partial v}{\partial h} \right)^2}, \quad (14)$$

where  $u$  and  $v$  denote the north-south and east-west wind components, respectively.

## 3. Validation Experiment

### 3.1. Balloon-Borne Microthermal Measurement

For visible and near-infrared wavelengths, random fluctuations of the refractive index primarily occur due to temperature effects. In the inertial subdomain of the atmosphere,

$C_T^2$ , the temperature structure coefficient, is the proportional constant of the temperature structure function  $D_T(r)$  [34], which is expressed as:

$$C_T^2(r, h) = \frac{D_T(r, h)}{r^{2/3}}, \quad l_0 \ll r \ll L_0, \quad (15)$$

where  $D_T(r, h)$  denotes the temperature structure function,  $r$  (in m) represents the separation distance between a pair of microthermal probes, and  $h$  (in m) denotes the height of a separate microthermal probe.  $l_0$  and  $L_0$  correspond to the inner and outer scales of atmospheric turbulence, respectively. The temperature structure function is a statistic that describes temperature disturbance from a pair of temperature probes separated by distance  $r$ , which is given by

$$D_T(r, h) = \langle [T(p_1) - T(p_2)]^2 \rangle, \quad l_0 \ll r \ll L_0, \quad (16)$$

where  $T$  (in K) denotes the air temperature, the angle bracket  $\langle \rangle$  represents the ensemble average, and  $p_1$  and  $p_2$  denote the positions of the microthermal probes. The device employed sensor elements of a platinum wire with a 10  $\mu\text{m}$  diameter. Two-wire probes were spaced 1 m apart in a horizontal plane to sense temperature differences as the instrument ascends through the atmosphere at approximately  $5 \text{ m}\cdot\text{s}^{-1}$ . The platinum wire probes sense the temperature difference owing to the atmospheric temperature change and further respond to resistance. A pair of sensor wires can be considered as two legs of a Wheatstone bridge. Later, a rapidly varying voltage is generated due to the differences in probe resistance-temperature coefficients. The response frequency of the sensor is 0.05–30 Hz, and the electronic processing of signals corresponded to a temperature difference of 0.002 K, which conforms with the internationally used technical indicators [35–38].

Beland expressed the relationship between  $C_n^2(h)$  and  $C_T^2(r, h)$  by considering the Gladstone formula [39], the refractive index structure constant  $C_n^2(h)$  can be expressed in terms of  $C_T^2(r, h)$ :

$$C_n^2(h) = \left[ 79 \times 10^{-6} \frac{P(h)}{T^2(h)} \right]^2 C_T^2(r, h), \quad (17)$$

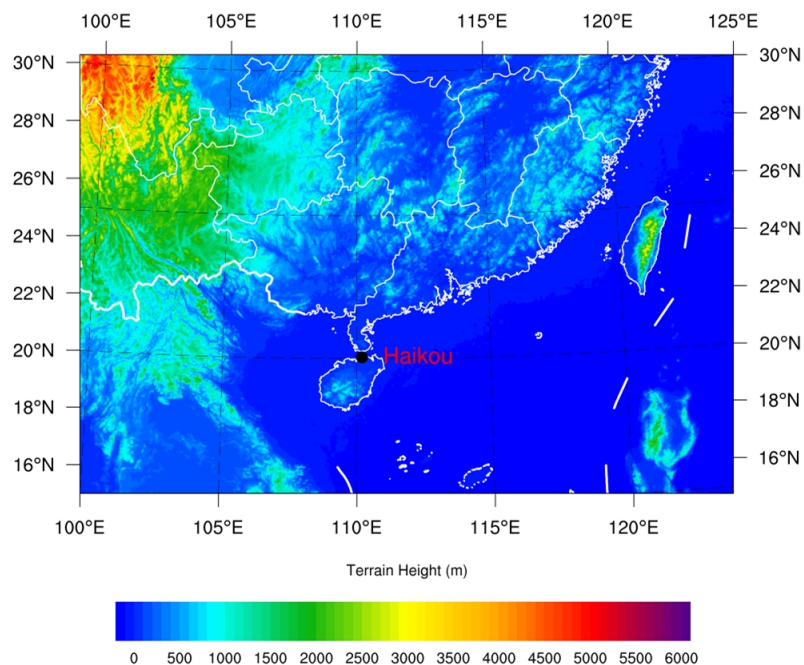
where  $P$  (in hPa) denotes the air pressure. The balloon-borne microthermal measurement system provides  $C_T^2(h)$  data by measuring the mean square temperature fluctuations from Equations (15) and (16) and thus  $C_n^2(h)$  can be acquired using Equation (17).

### 3.2. Field Campaign and Dataset

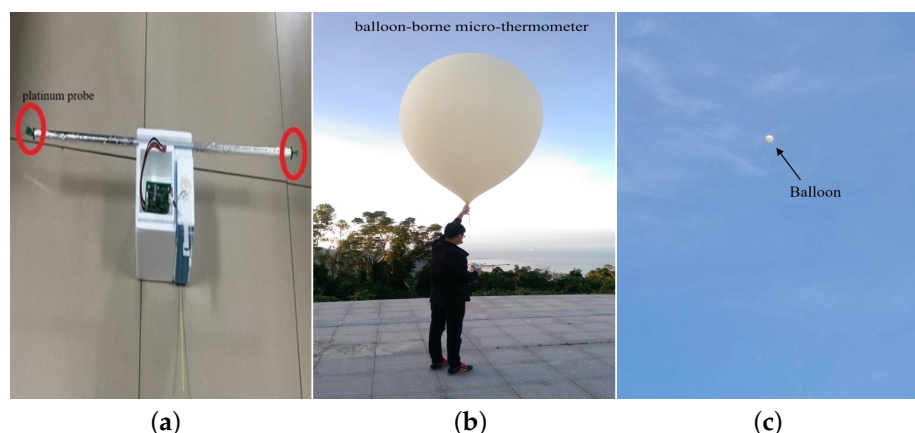
In this study, sounding measurements were conducted at the Haikou marine environment site from March to April in 2018. The Haikou site is located in the northern part of Hainan Island, facing the sea to the north and it has a tropical monsoon climate. The annual average precipitation is 2067 mm, while the annual average air temperature is 24.3 °C, the highest average temperature is approximately 28 °C, and the lowest average temperature is approximately 18 °C. The perennial wind direction is dominated by the southeast and northeast winds, and the annual average wind speed is  $3.4 \text{ m}\cdot\text{s}^{-1}$ . The field campaign site and terrain height at the Haikou site are shown in Figure 5.

Figure 6 shows the balloon-borne microthermal measurement experiment. Figure 6a illustrates the micro-thermometer of the balloon-borne microthermal measurement system. In the experiment, the micro-thermometer was attached to a meteorological sounding and was carried into the atmosphere by a balloon. Moreover, the balloon-borne payload was attached to other meteorological radiosondes, such as a temperature sensor and an air pressure sensor. The information about wind velocity, wind direction, pressure, temperature, and humidity was also transmitted to the ground station in real time. The details of measuring devices are illustrated in Table 1. In a single-sounding experiment, the high-resolution profiles data, such as temperature, wind speed, and air pressure from the surface through a vertical extent of approximately 30 km above ground level (a.g.l) was acquired. During

the soundings, sometimes data were missing or abnormal with insufficient height due to various factors, such as weather and damage caused by strong winds. After eliminating abnormal data, 21 available data were reserved, including 9 sounding data in the morning and 12 in the night. The available microthermal measurements are listed in Table 2.



**Figure 5.** Topographical distribution map of Haikou marine environment site. The black point represents the Haikou radiosonde station.



**Figure 6.** (a) Payload of balloon-borne micro-thermometer measurement system. (b) Balloon-borne micro-thermometer measurement. (c) Balloon.

**Table 1.** The details of measuring devices.

Parameter	Measuring Range	Accuracy
Temperature	−90–50 °C	0.2 °C
Pressure	5–1060 hPa	0.3 hPa
Wind speed	0–150 m·s <sup>−1</sup>	0.3 m·s <sup>−1</sup>
Wind Direction	0–360°	3°
Turbulence	10 <sup>−20</sup> –10 <sup>−12</sup> m <sup>−2/3</sup>	10 <sup>−18</sup> m <sup>−2/3</sup>

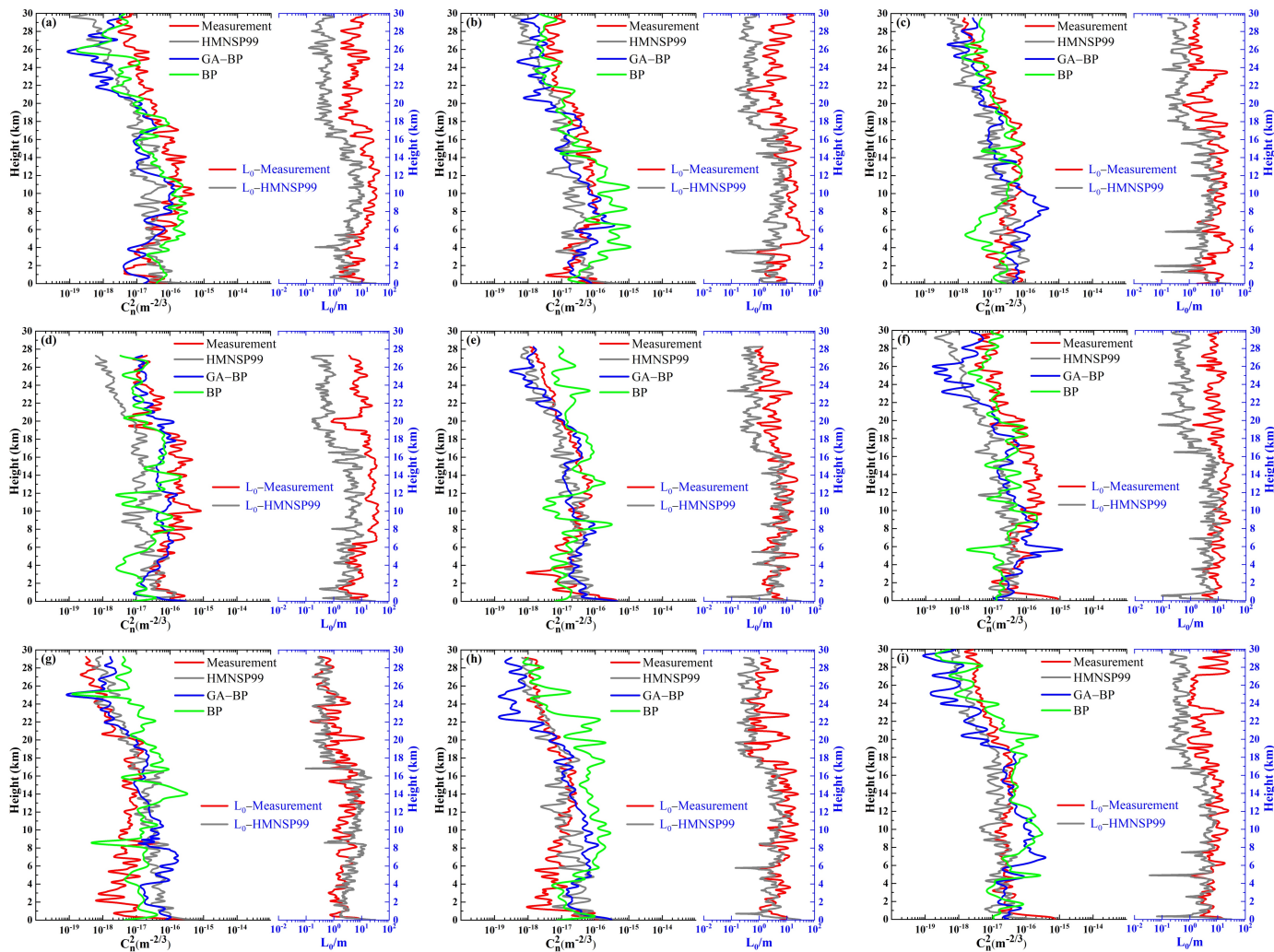
**Table 2.** A total of 21 results of the balloon-borne microthermal measurement field campaigns at Haikou marine environment site from March to April in 2018. The height a.g.l, launch date, time, and termination time are listed (note: the date and time reported were the local date and time).

Flight Number	Launch Date (LT)	Launch Time (LT)	Termination Time (LT)	Termination Altitude (m)
1	28 March 2018	19:58	21:18	29,860
2	29 March 2018	20:01	21:23	32,030
3	1 April 2018	07:44	09:06	30,230
4	1 April 2018	20:15	21:42	31,150
5	2 April 2018	19:50	21:25	32,590
6	3 April 2018	07:50	09:19	30,070
7	3 April 2018	19:50	21:05	27,860
8	8 April 2018	07:52	09:22	29,500
9	9 April 2018	19:50	21:06	28,770
10	10 April 2018	20:00	21:37	33,030
11	11 April 2018	08:00	09:18	27,290
12	12 April 2018	08:00	09:23	28,270
13	13 April 2018	20:00	21:34	32,510
14	14 April 2018	08:00	09:29	30,360
15	20 April 2018	08:00	09:18	29,250
16	20 April 2018	20:01	21:28	30,410
17	21 April 2018	20:01	21:29	31,490
18	22 April 2018	08:00	09:27	29,150
19	22 April 2018	20:00	21:32	31,650
20	23 April 2018	08:00	09:25	32,250
21	27 April 2018	01:40	02:57	28,210

## 4. Results

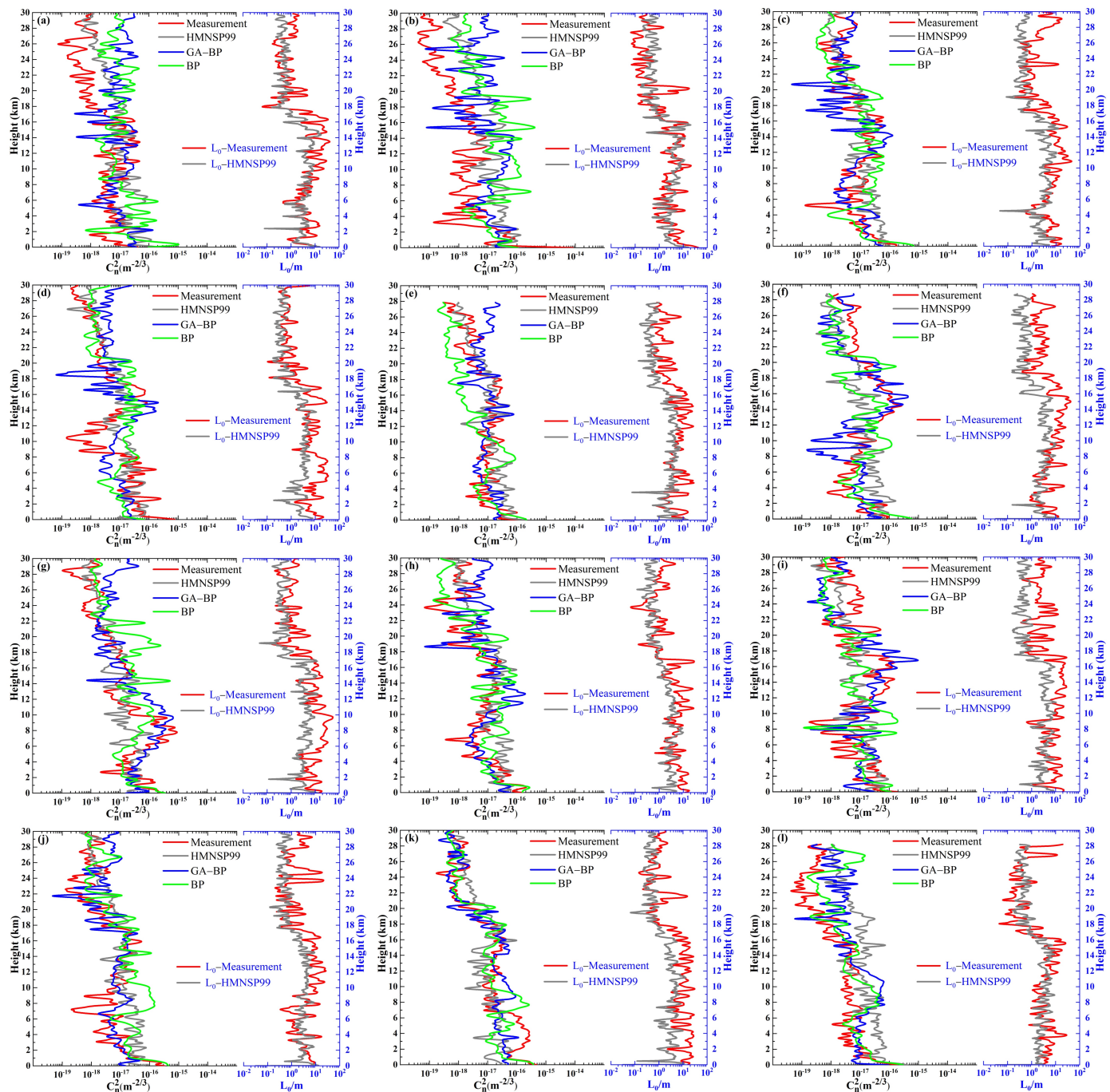
### 4.1. Estimation of $C_n^2(h)$ Profiles

Figure 7 presents the comparison of the individual  $C_n^2(h)$  profiles obtained by the GA-BP, BP and HMNSP99 models, along with the corresponding individual measured  $C_n^2(h)$  profiles in the morning. In addition, the  $L_0(h)$  vertical profiles from the HMNSP99 model and measurements are also illustrated in Figure 7. Clearly, the  $L_0(h)$  vertical profiles from the HMNSP99 model and the measurement have a similar variation trend. On the other hand, the  $C_n^2(h)$  profiles from three models and the measurements decrease steeply in the surface layer, before gradually increasing up to the tropopause region, and then gradually decreases in the upper stratosphere, which is similar to the turbulence characteristics in the Hawaii marine environment [40,41]. It is worth highlighting that  $C_n^2(h)$  spikes are discernible and correspond to the tropopause at approximately 17 km a.g.l., whereas much less than an order difference between the three models and the measurement can be seen. However,  $C_n^2(h)$  values are underestimated, particularly above 20 km except for some profiles from the BP model. Overall, these results indicate that although the small-scale fluctuations are not captured, the models including the BP, GA-BP and the physically-based models can generally reflect the turbulence characteristics in variation trend and order of magnitude.



**Figure 7.** (a–i) Comparison of the  $C_n^2(h)$  profiles (left) between the models (GA-BP, BP and HMNSP99) and the measurement, the  $L_0(h)$  profiles (right) from the HMNSP99 model and the measurement in the morning.

Figure 8 shows the comparison of the  $C_n^2(h)$  profiles between the models (GA-BP, BP and HMNSP99) and the measurement, the  $L_0(h)$  vertical profiles from the HMNSP99 model and the measurements overnight. From the display, one can see that the  $L_0(h)$  vertical profiles from model are generally coherent with the measurement in trend and magnitude. Additionally, the visualization of  $C_n^2(h)$  profiles presents that almost all the  $C_n^2(h)$  profiles estimated by three models and the corresponding measurements are in fair visual agreement, particularly in the lower atmosphere. The  $C_n^2(h)$  profiles measured and estimated have a similar variation trend. One can see that the  $C_n^2(h)$  profiles reveal a steep drop close to the ground. It is followed by an increase in turbulence with altitudes in the troposphere and then a gradual decrease above the tropopause. It was found that the observed  $C_n^2(h)$  exhibits a spike at about 17 km a.g.l., which is qualitatively captured by the GA-BP model. However, such a sharp increase in  $C_n^2(h)$  is not picked up by the HMNSP99 model and the BP model in Figure 8f,i. The GA-BP model captures more details and generally agrees well with the measured values both in magnitude and trend. Obviously, the spikes and activity layers occur near the tropopause region. The differences between the three models and the measurement are relatively small when entering the tropopause region, including more obvious between about 17 km and 24 km, except for Figure 8a,b,l.



**Figure 8.** (a–l) Comparison of the  $C_n^2(h)$  profiles (left) between the models (GA-BP, BP and HMNSP99) and the measurement, the  $L_0(h)$  profiles (right) from the HMNSP99 model and the measurement in the night.

#### 4.2. Error Analysis

The integrated parameters include the Fried parameter ( $r_0$ ), isoplanatic angle ( $\theta_{AO}$ ), and the coherence time ( $\tau_{AO}$ ), which are crucial for the design and optimization of Adaptive Optics (AO) systems, derived from the vertical distribution of the refractive-index structure constant and the wind speed [42,43]. The  $r_0$ , also known as the coherence length, is the limiting aperture beyond which an increase in aperture diameter does not cause an increase in resolution. Furthermore,  $\theta_{AO}$  is defined as the maximum angular that can maintain phase coherence between two measurement points for the same observation target. If beyond the range of  $\theta_{AO}$ , the phase screen measurement performed will change greatly. Additionally,

$\tau_{AO}$  indicates how long the wavefront remains coherent, the large wavefront coherence time determines the response parameters of the AO system design. The integrated parameters are expressed using the formula as follows:

$$r_0 = \left[ 0.423 \left( \frac{2\pi}{\lambda} \right)^2 \int_0^\infty C_n^2(h) dh \right]^{-3/5}, \quad (18)$$

$$\theta_{AO} = 0.057\lambda^{6/5} \left[ \int_0^\infty C_n^2(h) h^{5/3} dh \right]^{-3/5}, \quad (19)$$

$$\tau_{AO} = 0.057\lambda^{6/5} \left[ \int_0^\infty C_n^2(h) |V(h)|^{5/3} dh \right]^{-3/5}, \quad (20)$$

where  $V(h)$  denotes the wind speed as a function of altitude  $h$ .  $\lambda$  represents a given wavelength (500 nm), and all the integrated parameters are referred to the zenith direction.

The statistical operators including the bias and the root-mean-squared error (RMSE) are used to analyze the correlation between the measured and estimated values of the radiosonde to evaluate the reliability of the BP, GA-BP neural network, and HMNSP99 models [44]. The definition of the statistical operators is given as follows:

$$Bias = \sum_{i=1}^N \frac{Y_i - X_i}{N}, \quad (21)$$

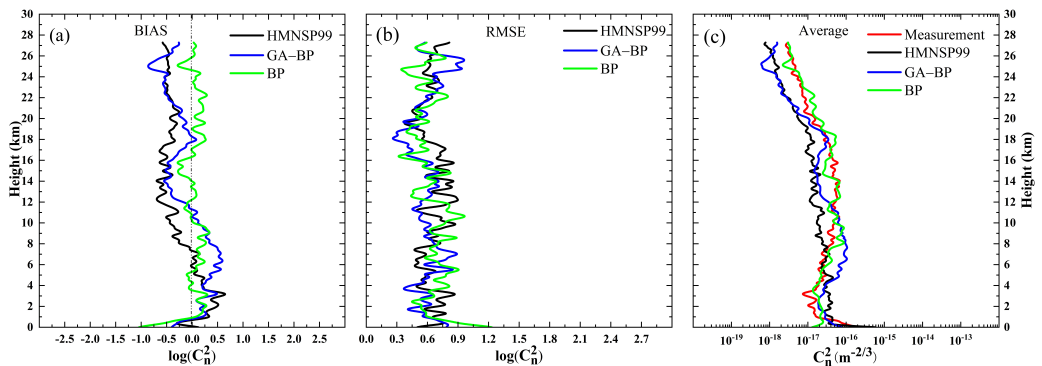
$$RMSE = \sqrt{\sum_{i=1}^N \frac{(Y_i - X_i)^2}{N}}, \quad (22)$$

where  $X_i$  denotes the individual measured values,  $Y_i$  denotes the individual values estimated by the model at the same height.  $N$  represents the number of samples for a couple  $(X_i, Y_i)$  at the same height.  $\bar{X}_i$  and  $\bar{Y}_i$  correspond to the average value of measured and the estimated, respectively.

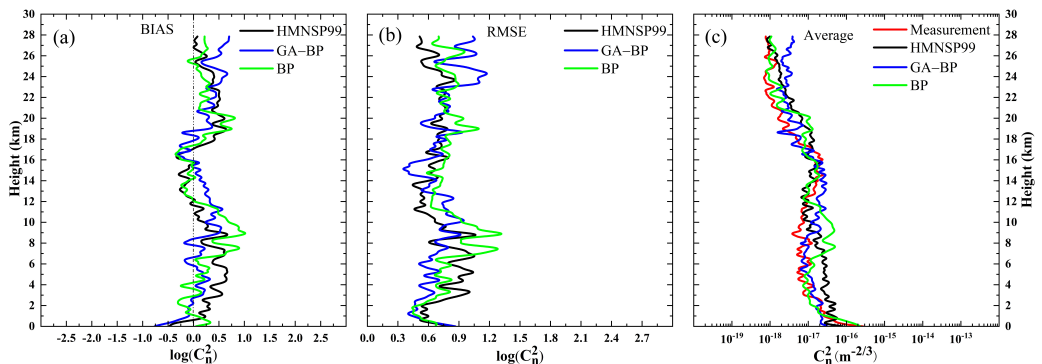
The comparisons of statistical operators between the  $C_n^2(h)$  profiles produced by estimations and measurements are clearly illustrated in Figures 9 and 10 to evaluate the performances of the three models. Figure 9 shows the statistical results from three models and measurements in the morning. The bias values between three models and measurements are within  $1 \text{ m}^{-2/3}$ . Note that the bias values are closer to 0, indicating that the estimated model has better performance overall. It is clearly visible that the BP model and GA-BP model exhibit somewhat better performance in the high troposphere and low stratosphere. Moreover, the RMSE values reflect how spread out these prediction errors are. The RMSE values from the BP model show that the prediction deviates from the measurements at some altitudes in the troposphere which can be seen in Figure 7. Figure 9c displays the comparison of the estimated average  $C_n^2(h)$  profiles from three models and measurements in the morning. In general, it was found that the average  $C_n^2(h)$  profiles exhibited a similar variation trend and magnitude in the morning. However, the results reveal that the  $C_n^2(h)$  profiles estimated by the BP and GA-BP models are generally in good agreement with the measurement near the tropopause region.

Figure 10 illustrates the statistical results of the bias and RMSE for analyzing the correlation between the estimated  $C_n^2(h)$  values from three models and measurements in the night. It is evident from the statistical operators of  $\log[C_n^2(h)]$  from three models that the bias values are within  $1 \text{ m}^{-2/3}$  and that RMSE values are within  $1.4 \text{ m}^{-2/3}$ . Moreover, the GA-BP model has somewhat better performance in the low troposphere and low stratosphere. This phenomenon is evident in Figure 8. For the description of RMSE, the variation trend of RMSE values reflects that the BP model and GA-BP model have similar laws as bias values. Furthermore, Figure 10c presents the estimated average  $C_n^2(h)$  profiles from three models, along with the corresponding measurement in the night. Notably,

the average  $C_n^2(h)$  profiles from the GA-BP model are indeed closer to the measurement, although BP and HMNSP99 models still perform better at some heights. Overall, the statistical results over the entire altitude range show that estimated values from three models are coherent with the measurement in the Haikou at night, which presents the intrinsic ability to capture layers of high optical turbulence. Additionally, by comparison, one can see that the turbulence characteristics in the night at this location differ from an astronomical observatory site such as Mount Graham. For example, the strongest  $C_n^2(h)$  peak at Mt Graham occurred near the boundary layer, and the second peak was located between 9–11 km [45].



**Figure 9.** Statistical results of the  $C_n^2(h)$  profiles between the GA-BP, BP and HMNSP99 models in the morning. (a) BIAS. (b) RMSE. (c) Average  $C_n^2(h)$  profiles.



**Figure 10.** Statistical results of the  $C_n^2(h)$  profiles between the GA-BP, BP and HMNSP99 models in the night. (a) BIAS. (b) RMSE. (c) Average  $C_n^2(h)$  profiles.

The integrated turbulence parameters include  $r_0$ ,  $\theta_{AO}$ , and  $\tau_{AO}$  for adaptive optics systems applications derived from the  $C_n^2(h)$  profiles using the GA-BP, BP, HMNSP99 models and the measured  $C_n^2(h)$  profiles. The comparison of the integrated parameters is illustrated in Figure 11. It can be observed that  $r_0$ ,  $\theta_{AO}$ , and  $\tau_{AO}$  between the GA-BP, BP models and the measurement are generally consistent with each other except for some cases. The bias comparison of integrated parameters between GA-BP and BP models are listed in Table 3. As shown in Table 3, the  $r_0$  bias values of the GA-BP model are closer to zero compared to the BP model as a whole, indicating the integrated parameters from the GA-BP model generally show a good ability in reconstructing the distribution of the  $r_0$ ,  $\theta_{AO}$ , as well as  $\tau_{AO}$ . In addition, the BP network optimized by the genetic algorithm has better prediction ability, better global search ability, good robustness, and quick training speed, whereas the GA-BP model performs better than the BP model.

As shown in Figure 12, the statistical results for each integrated parameter between models (GA-BP, BP and HMNSP99) and the measurement are visually represented using a box plot. From the displays, the median values of  $r_0$ ,  $\theta_{AO}$ , and  $\tau_{AO}$  from the measurement are 9.94 cm, 0.69'', and 2.85 ms, respectively. The corresponding median  $r_0$ ,  $\theta_{AO}$ , and  $\tau_{AO}$  from the GA-BP model are 8.88 cm, 0.51'', and 1.96 ms, respectively, and the corresponding

median  $r_0$ ,  $\theta_{AO}$ , and  $\tau_{AO}$  from the BP model are 8.83 cm,  $0.53''$ , and 1.79 ms, respectively. Additionally, the median values of  $r_0$ ,  $\theta_{AO}$ , and  $\tau_{AO}$  from HMNSP99 model are 11.72 cm,  $0.85''$ , and 3.20 ms, respectively. The box plot for integrated parameters visualizes the general distribution of integrated parameters at the Haikou site, thus providing a potential value for the application of electro-optical systems in marine environments.

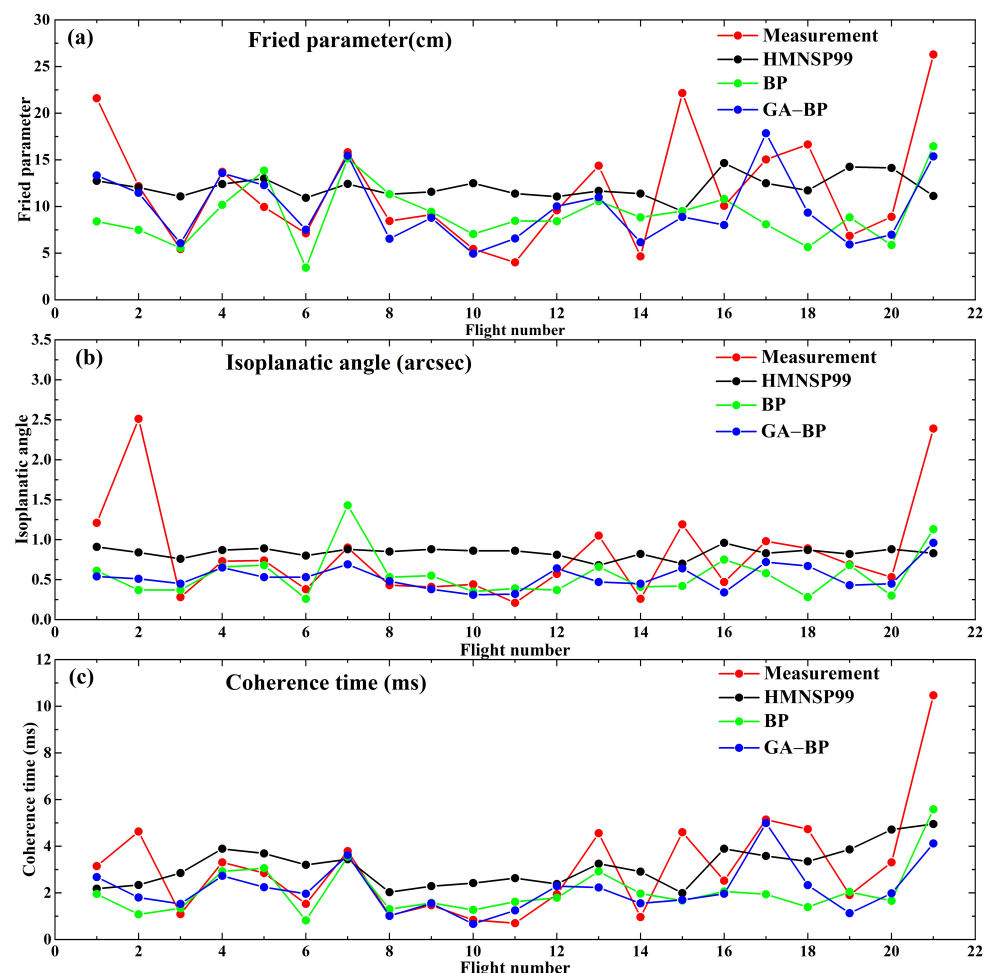


**Figure 11.** Comparison of the integrated parameters between GA-BP, BP and HMNSP99 models. (a) Fried parameter. (b) Isoplanatic angle. (c) Coherence time.

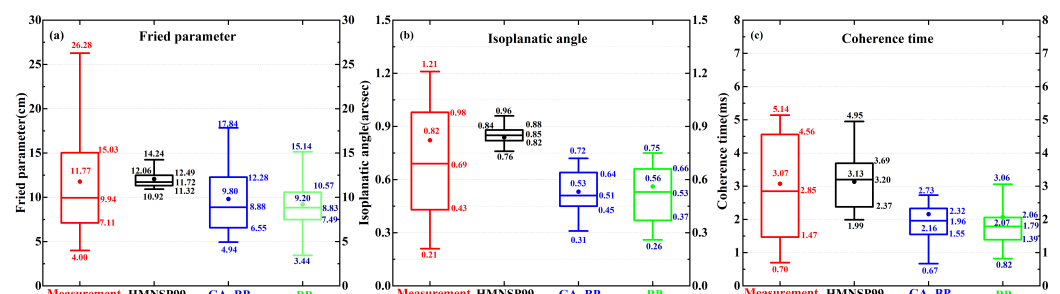


**Figure 12.** Box plot for integrated parameters between GA-BP, BP and HMNSP99 models. (a) Fried parameter. (b) Isoplanatic angle. (c) Coherence time.

**Table 3.** Comparison of integrated parameters between GA-BP and BP models. *BIAS* = Model – Measurement.

Flight Number	$r_0$ ( <i>BIAS</i> )		$\theta_{AO}$ ( <i>BIAS</i> )		$\tau_{AO}$ ( <i>BIAS</i> )	
	BP	GA-BP	BP	GA-BP	BP	GA-BP
1	−13.19	−8.27	−0.6	−0.67	−1.2	−0.47
2	−4.69	−0.72	−2.14	−2	−3.55	−2.83
3	0.12	0.63	0.09	0.17	0.25	0.44
4	−3.55	−0.14	0.07	−0.08	−0.39	−0.58
5	3.91	2.34	−0.06	−0.21	0.21	−0.61
6	−3.67	0.39	−0.12	0.15	−0.71	0.43
7	−0.66	−0.37	0.53	−0.21	−0.24	−0.17
8	2.87	−1.97	0.1	0.05	0.26	−0.03
9	0.3	−0.35	0.14	−0.03	0.1	0.08
10	1.6	−0.5	−0.09	−0.13	0.43	−0.17
11	4.45	2.56	0.18	0.11	0.92	0.55
12	−1.18	0.42	−0.2	0.07	−0.15	0.35
13	−3.79	−3.38	−0.39	−0.58	−1.64	−2.33
14	4.19	1.52	0.15	0.19	1.01	0.59
15	−12.63	−13.26	−0.77	−0.55	−2.93	−2.9
16	0.72	−2.06	0.28	−0.13	−0.46	−0.56
17	−6.94	2.81	−0.4	−0.26	−3.2	−0.15
18	−11	−7.3	−0.61	−0.22	−3.34	−2.4
19	1.98	−0.93	−0.01	−0.26	0.13	−0.78
20	−3.02	−1.92	−0.23	−0.08	−1.65	−1.33
21	−9.84	−10.92	−1.26	−1.43	−4.89	−6.35

## 5. Discussion

From the previous analysis in Section 4, the estimated  $C_n^2(h)$  from physically-based (HMNSP99) and neural network models exhibit some deviations from the measurements at some altitudes. The possible causes of the deviations and the improvements will be presented.

In reality, there exists intermittent turbulence or large uncertainties that trigger turbulence so that the value of  $C_n^2(h)$  measured by the micro-thermometer may not be the “true”  $C_n^2$  values. In addition, the  $C_n^2(h)$  profiles measurements may be influenced by some unknown factors in the marine environment. Notably, although the HMNSP99 model contains more meteorological parameters such as temperature gradients in addition to wind shear, it is not developed only for the maritime environment. The mechanism of turbulence will be continually explored and we intend to explore the more accurate physical estimating model in the marine environment.

Compared with the classic BP neural network, the genetic algorithm was used to optimize the initial connection weights and thresholds of the BP model to improve the global search ability, training speed, and good robustness of the network. However, the estimated results by the GA-BP model show no significant improvement. In fact, there is no systematic theory to determine the topological structure of the neural network and select appropriate input parameters. In addition, the sample data in this study (during March and April 2018) are limited and it is necessary to study the performance of the model used to forecast atmosphere turbulence in other time periods or other sites in marine environments. More field campaigns of sounding measurements will be carried out in marine environments to enrich the datasets and further study and verify the universality of the model, as well as further explore the main factors that influence the measurement. Moreover, the  $C_n^2(h)$  profiles from other measurement techniques such as DIM LIDAR can be acquired to validate the results. Additionally, we intend to optimize the design of the neural network by selecting more meteorological parameters, which are based on the physical process in the turbulence mechanism. Moreover, feature selection can be performed to select the best appropriate meteorological parameters for the neural

network model such as Jellen [46] to improve the accuracy of estimating  $C_n^2(h)$  profiles in marine environments.

## 6. Conclusions

In this study, the GA-BP model was developed to estimate  $C_n^2(h)$  profiles in the Haikou marine environment. First, the  $C_n^2(h)$  profiles estimated by the traditional physically-based (HMNSP99) model, BP model, and GA-BP model were compared with the corresponding sounding measurement. Subsequently, the performance of the three models was evaluated using the statistical operators. Moreover, we analyzed the main integrated parameters ( $r_0$ ,  $\theta_{AO}$  and  $\tau_{AO}$ ) that contain fundamental information in the adaptive optics optimization. The results obtained by the estimation of three models are summarized as follows.

The estimated  $C_n^2(h)$  profiles from the HMNSP99 and GA-BP models are slightly smaller than the measured values above 20 km in the morning in the Haikou marine environment. In addition, almost all  $C_n^2(h)$  profiles estimated by three models and the corresponding measured  $C_n^2(h)$  profiles at night are in fair visual agreement, particularly in the lower atmosphere. The differences between the three models and the measurement are relatively small when entering the tropopause region except for some soundings. Additionally, at some altitudes, the GA-BP model demonstrates its capabilities by capturing the detailed changes of  $C_n^2(h)$  remarkably well compared to BP and HMNSP99 models. For the statistical results of integrated parameters, the integrated astronomical parameters from the GA-BP model are more reasonable in general compared to the BP model. The fidelity of  $C_n^2(h)$  turbulence profiles and the integrated astronomical parameters in marine environments indicate that the GA-BP model presents a novel idea to estimate  $C_n^2(h)$  profiles in marine environments. Moreover, the median  $r_0$ ,  $\theta_{AO}$ , and  $\tau_{AO}$  calculated from the measured  $C_n^2(h)$  profiles are 9.94 cm, 0.69'', and 2.85 ms, respectively, which provide independent optical turbulence parameters for adaptive optics systems in marine environments.

In summary, the GA-BP model can describe the characteristics of the vertical distributions of  $C_n^2(h)$  profiles and the main integral parameters in marine environments. Although the estimated  $C_n^2(h)$  profiles from the model are not completely consistent with the measured values at each altitude, the results achieved in this study provide useful information for designing, monitoring, and even optimizing the performance of optoelectronic systems in marine environments.

**Author Contributions:** Conceptualization, C.B., C.Q. and W.Z.; methodology, C.B., C.Q., P.W. and W.Z.; validation, Q.L., X.Q., N.W. and W.Z.; data analysis, C.B., C.Q., X.J. and Q.L.; writing—original draft preparation, C.B.; writing—review and editing, C.B., X.J. and C.Q. All authors have read and agreed to the published version of the manuscript.

**Funding:** This work is supported by the Foundation of Advanced Laser Technology Laboratory of Anhui Province (Grant No. AHL2021QN02) and Foundation of Key Laboratory of Science and Technology Innovation of Chinese Academy of Sciences (Grant No. CXJJ-21S028).

**Data Availability Statement:** In this section, the data underlying this article cannot be shared publicly due to the confidentiality requirements of the project in the study.

**Acknowledgments:** The authors would like to thank Xin Zheng for preparing and launching the radiosonde measurement.

**Conflicts of Interest:** The authors declare no conflict of interest.

## References

1. Tatarskii, V.I. *Wave Propagation in a Turbulent Medium*; McGraw-Hill: New York, NY, USA, 1961.
2. Good, R.E.; Beland, R.R.; Murphy, E.A.; Brown, J.H.; Dewan, E.M. Atmospheric models of optical turbulence. In Proceedings of the Modeling of the Atmosphere, Orlando, FL, USA, 4–8 April 1988; pp. 165–186.
3. Avila, R.; Vernin, J.; Masciadri, E. Whole atmospheric-turbulence profiling with generalized scidar. *Appl. Opt.* **1997**, *36*, 7898–7905. [[CrossRef](#)] [[PubMed](#)]

4. Kornilov, V.; Tokovinin, A.; Vozyakova, O.; Zaitsev, A.; Shatsky, N.; Potanin, S.; Sarazin, M. MASS: A monitor of the vertical turbulence distribution. In Proceedings of the Astronomical Telescopes and Instrumentation, Waikoloa, HI, USA, 22–28 August 2003; pp. 837–845.
5. Kornilov, V.; Tokovinin, A.; Shatsky, N.; Voziakova, O.; Potanin, S.; Safonov, B. Combined MASS–DIMM instruments for atmospheric turbulence studies. *Mon. Not. R. Astron. Soc.* **2007**, *382*, 1268–1278. [[CrossRef](#)]
6. Vernin, J.; Roddier, F. Experimental determination of two-dimensional spatiotemporal power spectra of stellar light scintillation Evidence for a multilayer structure of the air turbulence in the upper troposphere. *J. Opt. Soc. Am.* **1973**, *63*, 270–273. [[CrossRef](#)]
7. Wilson, R.W. SLODAR: Measuring optical turbulence altitude with a Shack–Hartmann wavefront sensor. *Mon. Not. R. Astron. Soc.* **2002**, *337*, 103–108. [[CrossRef](#)]
8. Butterley, T.; Wilson, R.W.; Sarazin, M. Determination of the profile of atmospheric optical turbulence strength from SLODAR data. *Mon. Not. R. Astron. Soc.* **2006**, *369*, 835–845. [[CrossRef](#)]
9. Vedrenne, N.; Michau, V.; Robert, C.; Conan, J.-M. Improvements in Cn2 profile monitoring with a Shack Hartmann Wavefront sensor. In Proceedings of the Atmospheric Optical Modeling, Measurement, and Simulation II, San Diego, CA, USA, 13–17 August 2006; p. 63030C.
10. Wang, Z.; Zhang, L.; Kong, L.; Bao, H.; Guo, Y.; Rao, X.; Zhong, L.; Zhu, L.; Rao, C. A modified S-DIMM+: Applying additional height grids for characterizing daytime seeing profiles. *Mon. Not. R. Astron. Soc.* **2018**, *478*, 1459–1467. [[CrossRef](#)]
11. Carlisle, E.; Schmidt, D.; Marino, J.; Guesalaga, A. Use of SLODAR for daytime turbulence profiling. In Proceedings of the Adaptive Optics for Extremely Large Telescopes, Tenerife, Canary Islands, Spain, 25–30 June 2017.
12. Sauvage, C.; Robert, C.; Mugnier, L.M.; Conan, J.-M.; Cohard, J.-M.; Nguyen, K.-L.; Irvine, M.; Lagouarde, J.-P. Near ground horizontal high resolution Cn2 profiling from Shack–Hartmann slopeand scintillation data. *Appl. Opt.* **2021**, *60*, 10499–10519. [[CrossRef](#)]
13. Laidlaw, D.J.; Reeves, A.P.; Singhal, H.; Calvo, R.M. Characterizing turbulence profile layers through celestial single-source observations. *Appl. Opt.* **2022**, *61*, 498–504. [[CrossRef](#)]
14. Gimmetstad, G.G.; Roberts, D.W.; Stewart, J.M.; Wood, J.W.; Eaton, F.D. Testing of LIDAR system for turbulence profiles. In Proceedings of the SPIE Defense and Security Symposium, Orlando, FL, USA, 16–20 March 2008; p. 695109.
15. Odintsov, S.L.; Gladkikh, V.A.; Kamardin, A.P.; Nevezorova, I.V. Determination of the Structural Characteristic of the Refractive Index of Optical Waves in the Atmospheric Boundary Layer with Remote Acoustic Sounding Facilities. *Atmosphere* **2019**, *10*, 711. [[CrossRef](#)]
16. Azouit, M.; Vernin, J. Optical Turbulence Profiling with Balloons Relevant to Astronomy and Atmospheric Physics. *Publ. Astron. Soc. Pac.* **2005**, *117*, 536–543. [[CrossRef](#)]
17. Hufnagel, R.E.; Stanley, N.R. Modulation Transfer Function Associated with Image Transmission through Turbulent Media. *J. Opt. Soc. Am.* **1964**, *54*, 52–61. [[CrossRef](#)]
18. Abahamid, A.; Jabiri, A.; Vernin, J.; Benkhaldoun, Z.; Azouit, M.; Agabi, A. Optical turbulence modeling in the boundary layer and free atmosphere using instrumented meteorological balloons. *Astron. Astrophys.* **2004**, *416*, 1193–1200. [[CrossRef](#)]
19. Nath, D.; Venkat Ratnam, M.; Patra, A.; Krishna Murthy, B.; Bhaskar Rao, S.V. Turbulence characteristics over tropical station Gadanki (13.5 N, 79.2 E) estimated using high-resolution GPS radiosonde data. *J. Geophys. Res.* **2010**, *115*, D07102. [[CrossRef](#)]
20. Dewan, E.M.; Good, R.E.; Beland, B.; Brown, J. *A Model for  $C_n^2$  (Optical Turbulence) Profiles Using Radiosonde Data*; Phillips Laboratory Technical Report, PL-TR-93-2043, ADA 279399; Phillips Laboratory: Albuquerque, NM, USA, 1993.
21. Ruggiero, F.H.; DeBenedictis, D.A. Forecasting optical turbulence from mesoscale numerical weather prediction models. In Proceedings of the DoD High Performance Modernization Program Users Group Conference, Austin, TX, USA, 1 January 2002; pp. 10–14.
22. Basu, S. A simple approach for estimating the refractive index structure parameter ( $C_n^2$ ) profile in the atmosphere. *Opt. Lett.* **2015**, *40*, 4130–4133. [[CrossRef](#)]
23. Tracey, B.D.; Duraisamy, K.; Alonso, J.J. A machine learning strategy to assist turbulence model development. In Proceedings of the 53rd AIAA aerospace sciences meeting, Kissimmee, FL, USA, 5–9 January 2015; American Institute of Aeronautics and Astronautics: Reston, VA, USA, 2015; p. 1287.
24. Pelliccioni, A.; Tirabassi, T. Air dispersion model and neural network: A new perspective for integrated models in the simulation of complex situations. *Environ. Model. Softw.* **2006**, *21*, 539–546. [[CrossRef](#)]
25. Lohani, S.; Glasser, R.T. Turbulence correction with artificial neural networks. *Opt. Lett.* **2018**, *43*, 2611–2614. [[CrossRef](#)]
26. Khashei, M.; Rafiei, F.M.; Bijari, M. Hybrid Fuzzy Auto-Regressive Integrated Moving Average (FARIMAH) Model for Forecasting the Foreign Exchange Markets. *Int. J. Comput. Int. Syst.* **2013**, *6*, 954–968. [[CrossRef](#)]
27. Gómez, S.L.S.; González-Gutiérrez, C.; Alonso, E.D.; Santos, J.D.; Rodríguez, M.L.S.; Morris, T.; Osborn, J.; Basden, A.; Bonavera, L.; González, J.G.N. Experience with artificial neural networks applied in multi-object adaptive optics. *Publ. Astron. Soc. Pac.* **2019**, *131*, 108012. [[CrossRef](#)]
28. Wang, Y.; Basu, S. Using an artificial neural network approach to estimate surface-layer optical turbulence at Mauna Loa, Hawaii. *Opt. Lett.* **2016**, *41*, 2334–2337. [[CrossRef](#)]
29. Su, C.D.; Wu, X.Q.; Luo, T.; Wu, S.; Qing, C. Adaptive niche-genetic algorithm based on backpropagation neural network for atmospheric turbulence forecasting. *Appl. Opt.* **2020**, *59*, 3699–3705. [[CrossRef](#)]

30. Xu, M.M.; Shao, S.Y.; Liu, Q.; Sun, G.; Han, Y.; Weng, N.Q. Optical Turbulence Profile Forecasting and Verification in the Offshore Atmospheric Boundary Layer. *Appl. Sci.* **2021**, *11*, 8523. [[CrossRef](#)]
31. Aslanargun, A.; Mammadov, M.; Yazici, B.; Yolacan, S. Comparison of ARIMA, neural networks and hybrid models in time series: Tourist arrival forecasting. *J. Stat. Comput. Simul.* **2007**, *77*, 29–53. [[CrossRef](#)]
32. Ranjithan, S.; Eheart, J.W.; Garrett, J.H., Jr. Neural network-based screening for groundwater reclamation under uncertainty. *Water Resour. Res.* **1993**, *29*, 563–574. [[CrossRef](#)]
33. Riedmiller, M.; Braun, H. A direct adaptive method for faster backpropagation learning: The RPROP algorithm. In Proceedings of the IEEE International Conference on Neural Networks, San Francisco, CA, USA, 28 March–1 April 1993; pp. 586–591.
34. Bufton, J.L. Correlation of microthermal turbulence data with meteorological soundings in the troposphere. *J. Atmos. Sci.* **1973**, *30*, 83–87. [[CrossRef](#)]
35. Qing, C.; Wu, X.Q.; Li, X.B.; Luo, T.; Su, C.D.; Zhu, W.Y. Mesoscale optical turbulence simulations above Tibetan Plateau: First attempt. *Opt. Express* **2020**, *28*, 4571–4586. [[CrossRef](#)]
36. Qing, C.; Luo, T.; Bi, C.C.; Li, X.B.; Cui, S.C.; Yang, Q.K.; Su, C.D.; Wu, S.; Qian, X.M.; Wu, X.Q. Optical turbulence and wind speed distributions above the Tibetan Plateau from balloon-borne microthermal measurements. *Mon. Not. R. Astron. Soc.* **2021**, *508*, 4096–4105. [[CrossRef](#)]
37. Bi, C.C.; Qian, X.M.; Liu, Q.; Zhu, W.Y.; Li, X.B.; Luo, T.; Wu, X.Q.; Qing, C. Estimating and measurement of atmospheric optical turbulence according to balloon-borne radiosonde for three sites in China. *J. Opt. Soc. Am. A* **2020**, *37*, 1785–1794. [[CrossRef](#)]
38. Han, Y.J.; Wu, X.Q.; Luo, T.; Qing, C.; Yang, Q.K.; Jin, X.M.; Liu, N.N.; Wu, S.; Su, C.D. New ( $C_n^2$ ) statistical model based on first radiosonde turbulence observation over Lhasa. *J. Opt. Soc. Am. A* **2020**, *37*, 995–1001. [[CrossRef](#)]
39. Beland, R.R. Propagation through atmospheric optical turbulence. *Atmos. Propag. Radiat.* **1993**, *2*, 157–232.
40. Basu, S.; Osborn, J.; He, P.; DeMarco, A. Mesoscale modelling of optical turbulence in the atmosphere: The need for ultrahigh vertical grid resolution. *Mon. Not. R. Astron. Soc.* **2020**, *497*, 2302–2308. [[CrossRef](#)]
41. McHugh, J.P.; Jumper, G.Y.; Chun, M. Balloon thermosonde measurements over Mauna Kea and comparison with seeing measurements. *Publ. Astron. Soc. Pac.* **2008**, *120*, 1318–1324. [[CrossRef](#)]
42. Masciadri, E.; Stoesz, J.; Hagelin, S.; Lascaux, F. Optical turbulence vertical distribution with standard and high resolution at Mt Graham. *Mon. Not. R. Astron. Soc.* **2010**, *404*, 144–158.
43. Roddier, F.; Gilli, J.M.; Lund, G. On the origin of speckle boiling and its effects in stellar speckle interferometry. *J. Opt.* **1982**, *13*, 263–271. [[CrossRef](#)]
44. Masciadri, E.; Lascaux, F.; Fini, L. MOSE: Operational forecast of the optical turbulence and atmospheric parameters at European Southern Observatory ground-based sites—I. Overview and vertical stratification of atmospheric parameters at 0–20 km. *Mon. Not. R. Astron. Soc.* **2013**, *436*, 1968–1985. [[CrossRef](#)]
45. Hagelin, S.; Masciadri, E.; Lascaux, F. Optical turbulence simulations at Mt Graham using the Meso-NH model. *Mon. Not. R. Astron. Soc.* **2011**, *412*, 2695–2706. [[CrossRef](#)]
46. Jellen, C.; Burkhardt, J.; Brownell, C.; Nelson, C. Machine learning informed predictor importance measures of environmental parameters in maritime optical turbulence. *Appl. Opt.* **2020**, *59*, 6379–6389. [[CrossRef](#)]